Cheng, Y. P., Bolton, M. D. & Nakata, Y. (2004). *Géotechnique* **54**, No. 2, 131–141

Crushing and plastic deformation of soils simulated using DEM

Y. P. CHENG*, M. D. BOLTON* and Y. NAKATA†

Cheng and co-workers showed how to make numerical simulations of crushable soils by the discrete element method (DEM). Stress-path tests on triaxial elements comprising crushable agglomerates have now been simulated. The plastic behaviour of this numerically generated soil closely resembles that of real sand. Crushing in the aggregate begins at stresses less than one tenth of the characteristic strength of single grains. The yield surfaces of isotropic 'lightly overconsolidated' DEM simulations are also contours of breakage, and are elliptical on Cambridge-style (q, p') plots and symmetrical about the p' axis. The points of maximum deviator stress at yield lie along lines of stress ratio $M_y = \pm 0{\cdot}8$, but the plastic strain increments at yield are non-associated, giving more contraction than normality would allow. Significantly, therefore, the stress ratio M_y was found not to coincide with critical states. All stress-path simulations yielding with $q/p' > M_y$ were found to satisfy the requirements of stress–dilatancy theory. In particular, their yielding was best described using a unique Mohr–Coulomb angle of internal friction ϕ, correlated with dilatancy rate. Points of zero dilation were found within this regime, providing a critical-state friction angle $\phi_{crit} = 42^\circ$ for these very 'rough' agglomerates. They also coincided with the location of a critical-state line on an e–$\log p'$ plot. The peak angle (ϕ_{peak}) developed in a variety of tests showed a unique correlation, reducing by progressive grain crushing as $\log \sigma'_1$ increased. As macroscopic stress levels approached the characteristic crushing strength of grains, it was impossible even to mobilise $\phi = \phi_{crit}$, owing to large strains and high degrees of breakage.

KEYWORDS: numerical modelling; stress path; particle crushing/crushability; deformation; friction; constitutive relations

Cheng et ses collègues ont montré comment faire des simulations numériques de sols écrasables par la méthode d'éléments discrets (DEM). Les essais de cheminement de contrainte sur des éléments triaxiaux comprenant des agglomérés écrasables ont maintenant été simulés. Le comportement plastique de ce sol créé numériquement ressemble de près à celui du vrai sable. L'écrasement dans l'agrégat commence à des contraintes inférieures à un dixième de la résistance caractéristique des grains simples. Les surfaces d'écoulement des simulations DEM isotropes 'légèrement surconsolidées' sont également les contours de la cassure et sont elliptiques sur les tracés de style Cambridge (q, p') et symétriques vers l'axe p'. Les points de contrainte déviatrice maximum à l'écoulement, se trouvent le long des lignes de taux de contrainte $My = +/- 0{,}8$, mais les augmentations de déformation plastique à l'écoulement ne sont pas associées, donnant plus de contraction que la normale le permettrait. De manière significative, le rapport de contrainte M_y s'est donc révélé ne coïncidant pas avec les états critiques. Toutes les simulations de cheminement de contrainte avec $q/p' > M_y$ sont apparues comme satisfaisant les exigences de la théorie contrainte/dilatance. En particulier, leur limite d'élasticité pouvait être décrite comme utilisant un angle unique Mohr-Coulomb de friction interne ϕ corrélatif au taux de dilatance. Des points de dilation zéro ont été trouvés dans ce régime, donnant un angle de friction d'état critique ϕ_{crit} de 42° pour ces agglomérés très 'grossiers'. Ils coïncidaient également avec l'emplacement d'une ligne d'état critique sur un tracé e-log p'. L'angle de crête (ϕ_{peak}) développé dans une variété de tests a montré une corrélation unique diminuant par écrasement de grain progressif à mesure que log σ'_1 augmentait. Étant donné que les niveaux de contrainte macroscopique s'approchaient de la résistance à l'écrasement caractéristique des grains, il a été impossible de mobiliser $\phi = \phi_{crit}$ à cause des grosses déformations et du haut degré de cassure.

INTRODUCTION

In science and engineering, the concept of yielding is used to divide elastic and plastic behaviours. In soil, this division is complicated by changes of internal voids ratio. A marked rate of change in the magnitude of voids ratio, e, with a change of effective mean stress, p' (or in the deviator shear strain, ε_q, with a change in the deviator stress, q), defines the yielding of soil. Geotechnical engineers still do not have a clear mental model of what yielding actually involves, however.

Simple elastic perfectly plastic models were developed in the 1960s. The Cambridge-type plasticity soil model first introduced by Roscoe *et al.* (1958) was partially empirical but based on continuum mechanics. The original Cam-clay model adopted normality as a flow rule and a purely frictional dissipation function that included a critical-state friction parameter, M (Roscoe *et al.*, 1963) to derive the shape of the yield surface (on the contractile or 'wet' side of critical states). Soil strength and plastic deformation, however, need not be solely frictional. Roscoe & Burland (1968) later formulated another dissipation function that included the effect of volumetric hardening. An elliptical yield surface was derived. Although they did not give the modification a clear physical explanation, it avoided any ambiguity in the direction of plastic flow increments in the region close to hydrostatic compression. On the other hand, the hysteretic behaviour of soil at small strains cannot be modelled by elastic perfectly plastic models. Mroz *et al.* (1979) introduced kinematic hardening into soil modelling and formulated a new type of model initially based on the idea of two nested yield surfaces. Jardine (1992) later categorised yielding using three surfaces at small, intermediate and large strain, each conveying aspects of plasticity observed in soil element tests.

The concepts of yield and plastic deformation, especially when all possible directions of stress-path loading are

Manuscript received 6 March 2003; revised manuscript accepted 3 December 2003.
Discussion on this paper closes on 1 September 2004, for further details see p. ii.
* Department of Engineering, Cambridge University, UK.
† Department of Civil Engineering, Yamaguchi University, Japan.

considered, deserve a reinterpretation within a granular perspective. This approach can clarify many of the postulated micro-mechanisms, from which improved plasticity models can be derived.

Bolton (1986) empirically related soil strength and dilatancy (on the dilatant or 'dry' side of critical states) with both stress level and density. A possible link between grain crushing and the dilatational component of the angle of internal friction was suggested. For many years, the importance of soil crushability to the basic plastic behaviour of soil had been well anticipated (Rowe, 1971; Chandler, 1985), yet it had been found difficult to quantify. Limitations still exist in the interpretation of laboratory tests because fundamental grain characteristics and interactions are unknown. New approaches, such as the discrete element method (DEM), can offer new insights.

The use of DEM in modelling the behaviour of crushable soil has aroused increasing attention since the crushability of soil grains was included in the modelling procedure. Following Robertson (2000), numerical 'grains' (agglomerates) can be made by bonding elementary spheres in probabilistically flawed 'crystallographic' arrays. McDowell & Harireche (2002) also validated the use of DEM in modelling soil particle fracture. Not only could DEM simulate the crushing strength of a real sand grain, with diametral breakage of the bonded agglomerates between flat platens, it could also reproduce realistic Weibull distributions of crushing strength in a batch of flawed agglomerates. Cheng *et al.* (2003) applied this DEM approach to simulate the compression and shearing behaviour of an element of crushable soil (silica sand) by reproducing the statistical crushing strength of a batch of uniformly sized 'grains' randomised by the removal of 20% of the microspheres (see Fig. 1(a)). They produced 389 numerical agglomerates using 17 274 spheres in their simulation. Following Robertson (2000), the contact normal and shear stiffness and the contact bond strength of each microsphere, 0·2 mm in diameter, were given values of 4 MN/m and 4 N respectively. The frictional coefficient at the surface of the microsphere is 0·5, equivalent to $\phi_\mu = 26{\cdot}6°$. Although the effect of particle size on the grain-crushing strength was not specifically modelled, reasonable agreement was found between the real data obtained from isotropically compressed silica sand and the DEM simulation when stress was normalised by the characteristic crushing strength of the grains (Fig. 1(b)). Cheng *et al.* (2003) went on to present a micromechanical interpretation for 'undrained' shearing tests. This paper is the continuation of the foregoing research, with particular focus on the fundamentals of yielding and plastic deformation. All input parameters of the numerical tests presented in this paper are identical to those of Cheng *et al.* (2003), and are shown in Table 1.

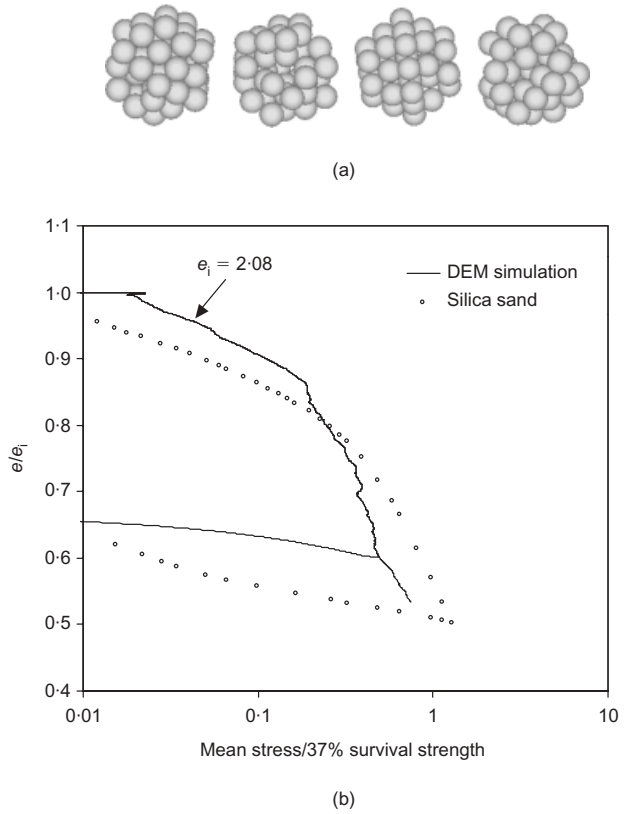

Fig. 1. (a) Examples of DEM agglomerates (Cheng *et al.*, 2003); (b) normalised voids ratio plotted against mean effective stress normalised by grain tensile strength (Cheng *et al.*, 2003)

CRUSHING

Yielding during isotropic compression

The macroscopic response (reduction of voids ratio) and microscopic response (percentage of broken bonds) of computer-simulated strain-rate-controlled isotropic compression tests on two DEM elements, with boundary walls approach-

Table 1 Information on an agglomerate (Cheng *et al.*, 2003)

Input parameter	Numerical value
Diameter of agglomerate: mm	1·0
Diameter of sphere: mm	0·2
Density of sphere: kg/m^3	2650
Maximum number of spheres in an agglomerate	57
Maximum number of bonds in an agglomerate	228
Normal and shear bond strength: N	4
Normal and shear stiffness of each sphere: N/m	4×10^6
Frictional coefficient of sphere	0·5
Percentage of spheres removed at random	20%

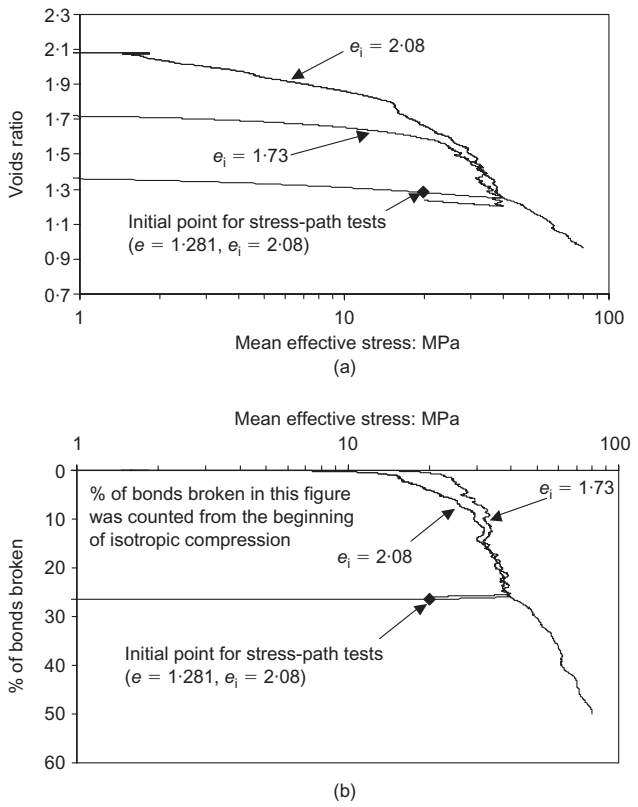

Fig. 2. Isotropic compression curves: (a) e–logp'; (b) pbb–logp'

ing at a relative speed of 2 m/s, are given in Fig. 2. The details of the modelling procedure can be found in Cheng *et al.* (2003) and are fully presented in Cheng (2004). Fig. 2(a) shows the conventionally defined voids ratio (the volume of voids divided by the volume of solids) plotted against the logarithm of mean effective stress. Microscopic information is given in Fig. 2(b), by plotting the percentage of simple contact bonds (that were used to build up the agglomerates) broken at each corresponding level of mean effective stress, relative to the total number of bonds that existed before the isotropic compression test. The counting of the percentage of broken bonds at each stage of a DEM simulation plays an important role in the micromechanical interpretation.

Figure 2 shows that the DEM soil with $e_i = 2{\cdot}08$ yielded twice, when the mean effective stress reached approximately 2 MPa and 15 MPa respectively. The insignificant change in volume in the initial portion of the curve ($p' < 2$ MPa) was due to pure elastic compression at contacts of elementary spheres. The 2 MPa yield point can be regarded as a pre-compression induced during sample formation. The subsequent reduction of voids before grains started crushing (at $p' > 7{\cdot}5$ MPa) was more significant, owing to rearrangement of the grains. The first instance of bond breakage was at 7·5 MPa. Crushing then increased progressively to about 15 MPa, after which there was a more marked rate of crushing against the logarithm of stress, associated with an approach to a 'normal compression line' in Fig. 2(a).

Bolton & Cheng (2001) show that the apparent yield point on an e–$\log p'$ plot can simply be an artefact of the use of a logarithmic axis to describe a linear (albeit plastic) compression due to occasional breakage and rearrangement, followed by clastic hardening. McDowell *et al.* (1996) describe as fractal compression the self-similar fracture of grain fragments that progressively fill voids as stress continues to increase, explaining the phenomenon of 'normal compression'. This phase of self-similar grain crushing and rearrangement can be inferred to apply to compression beyond about 15 MPa in Fig. 2(a). The compression test on a denser sample, with $e_i = 1{\cdot}73$, became fractal at a higher mean effective stress ($p' = 20$ MPa), the first instance of particle breakage having been at $p' = 15$ MPa, but it does approach the same 'normal compression line'.

Isotropic unloading of the DEM soils was allowed at $p'_{max} = 40$ MPa. A small amount of breakage could be seen in the initial stage of unloading, contributing to a hysteretic plastic strain accumulation during plastic unloading and reloading cycles. In this paper, monotonic stress-path shearing tests on an overconsolidated numerical soil are simulated and analysed. The DEM element (with $e_i = 2{\cdot}08$) was first loaded to 40 MPa and then unloaded to 20 MPa, giving an overconsolidation ratio defined with respect to p' of 2 ($n = 2$) before stress-path tests were simulated. This initial stress point prior to the stress-path tests is also shown in Fig. 2. Simulation of a specific stress-path direction was numerically obtained by using a servo algorithm that controlled the movement of the walls in relation to the stresses acting on them.

Yielding observed in q–p' space

The yield point was determined in the conventional way as a change in the slope of a stress–strain curve: Fig. 3(a) shows two examples. Given the stress–strain curve of a specific stress-path test, the data were first separated by lines of best fit to the pre-yield and post-yield behaviour; the yield point was determined to be the intersection of the lines. The process was repeated in the e–p' plot (Fig. 3(b)) to obtain the voids ratio corresponding to the same instances of yielding. Fig. 3(c) shows the corresponding yield points of all stress-path directions in q–p' space; yield points obtained in e–p' space are plotted in Fig. 5.

The yield points in effective stress space (Fig. 3(c)) lie on an elliptical yield surface, similar to the one derived from the modified Cam-clay (MCC) model, with $M_y = 0{\cdot}8$ in both compression and extension. As the apex of the ellipse had increased from 40 MPa at isotropic compression to 50 MPa on recompression, it seems that hardening had occurred owing to the unloading–reloading cycle. Yield at higher overconsolidation ratios occurred before the ellipse was reached. This was at stress ratios lying just beyond the two lines, $q = Fp'$, where $F_{comp} = 1{\cdot}72$ and $F_{ext} = -1{\cdot}09$, which correspond to the same mobilised angle of internal friction ($\phi = 42°$).

From the results of the stress-path shearing tests, the amount of bond breakage could be quantified by the percentage of broken bonds (pbb) counted from the beginning of shearing in each stress path. The pbb along each q–p' stress path is plotted in Fig. 4(a), in which the size of the bubbles indicates the amount of bond breakage. The stress paths end either when the pbb = 10%, or when strains exceeded 30%. In our simulations, the DEM elements were forced to deform uniformly at their boundaries and they contained only a small number of agglomerates, so localisation in shear band mechanisms was not observed.

When the element was sheared in stress paths that did not reach the F-lines, the pbb paths were characterised by a gradual increase in the size of the bubbles. Plastic irrecoverable strain accumulated continuously inside the original yield surface without any distinct jumps in the quantity of the pbb. On the other hand, paths that crossed the F-lines showed more sudden increases in breakage as they sheared to failure.

The numerical values of the pbb in a contour representation are shown in Fig. 4(b). The yield points obtained from the change-of-slope method (Fig. 3(c)) can be approximated by the 4% broken-bond contour (ppb = 4%). It is clearly seen that bond breakage occurred before gross plastic yielding could be detected in the stress–strain response. It is therefore clear that a significant proportion of bonds are broken as the stress state moves 'inside' the observed yield surface. Cracks propagate through many of the DEM 'grains', and the elastic response might be expected to degrade, but significant rearrangement (corresponding to macroscopic yielding) occurs only at about 4% pbb.

The contour at ppb = 0·1% represents an early threshold of damage and might be expected to move around with the initial stress state inside the bounding surface in the fashion of a kinematic yield surface. A three-zone yielding scheme was proposed by Jardine (1992) and Smith *et al.* (1992). The kinematic (Y_2) sub-yield surface of Bothkennar clay, reported by Smith *et al.* (1992), is shown in Fig. 4(c). It can be seen that the Y_2 yield surface in Fig. 4(c) and the 0·1 ppb surface in Fig. 4(b) are similar to one another. It is therefore suggested that the Y_2 surface is a threshold related to particle crushing, which can be used as an indicator of the onset of stiffness degradation. The Y_3 surface in Fig. 4(c) is also similar to the yield surface plotted in Fig. 3(c). However, Smith *et al.* (1992) used voids ratio to represent contours of yield surfaces, whereas we have used the pbb contours to represent them (Fig. 4(b)). These two representations are approximately the same so long as the 'elastic' response contributing to the slope of the κ-line is not significant. If the κ-value is not zero ($\kappa = 0{\cdot}04$ in our case; see Fig. 5), yield surfaces should not, in any event, be represented by constant voids ratio contours (Schofield & Wroth, 1968).

Additional comparison can be made with data for real sand presented by Gajo & Wood (1999), which was also discussed in the context of a kinematically hardening soil

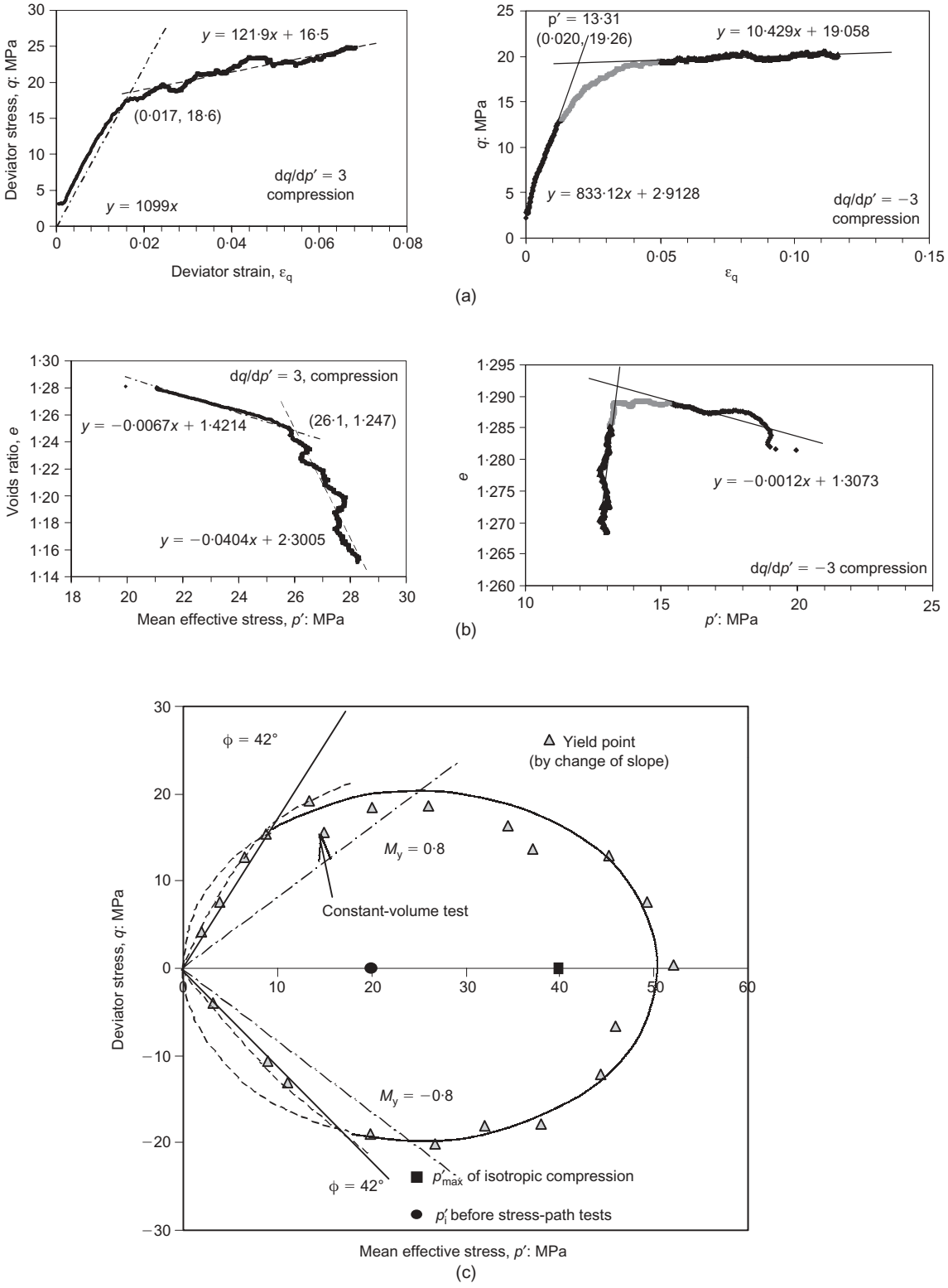

Fig. 3. A single yield surface obtained from 'change of slope': (a) curves of deviator stress against deviator strain; (b) curves of voids ratio against mean effective stress; (c) yield points in q–p' space

model (Mroz *et al.*, 1979). Gajo & Wood, however, made no comment about grain breakage in their kinematic hardening model, which may now be felt to be conceptually incomplete, following the DEM simulations.

Constant-volume compression can also easily be simulated; it is the non-linear path included in Fig. 4(a). The constant-volume test showed suppressed granular contraction, then suppressed dilation followed by contraction as particle crushing continued. The deviator stress (see label U) increased and then decreased, moving along the failure envelope while accumulating breakage. A detailed account of undrained compression tests on elements of DEM agglomerates can be found in Cheng *et al.* (2003).

Yielding observed in e–log p′ space

Figure 5 is a projection of the pbb contours in e–$\log p'$ space. The isotropic hardening parameter of the virgin com-

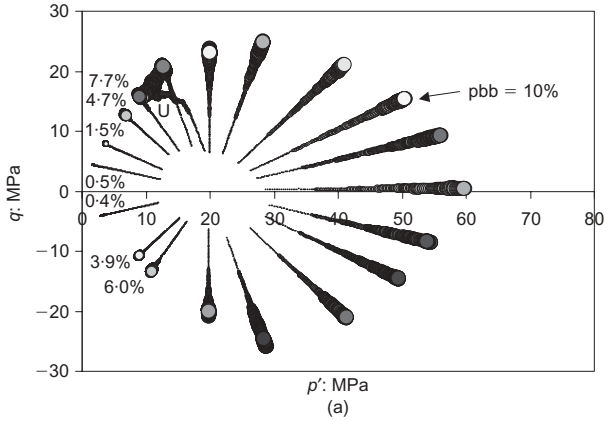

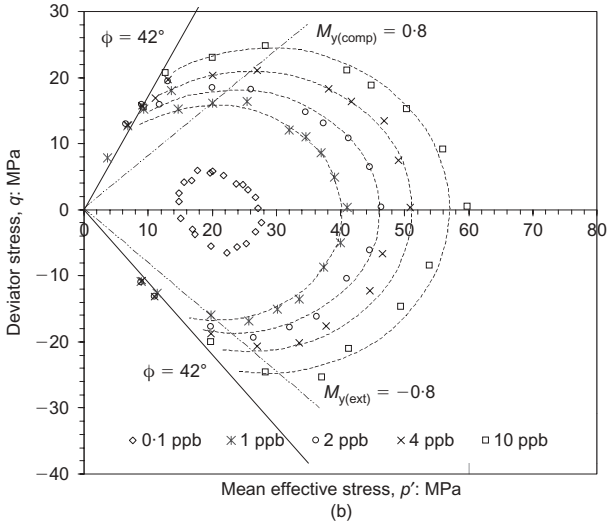

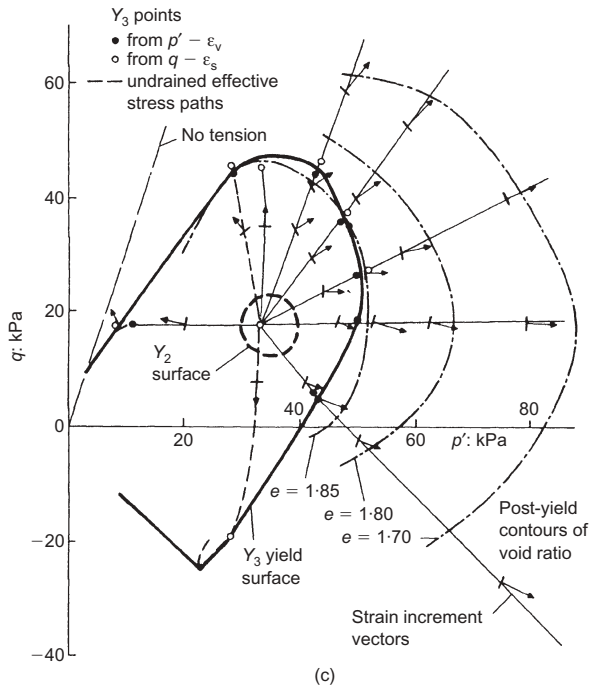

Fig. 4. Multiple yield surfaces in relation to particle breakage: (a) continuous breakage; (b) quantity and shape of pbb surfaces; (c) yielding characteristics of Laval sample of Bothkennar clay (Smith *et al.*, 1992)

pression line (λ) and the 'elastic' parameter (κ) of the unloading line could be reasonably calculated to be $\lambda = 0{\cdot}4$ and $\kappa = 0{\cdot}04$ in this stress range. The stress paths in e–$\log p'$ space are not as smooth as those shown in the q–p' space (Fig. 4(a)) except for the controlled constant-volume test. This unsteadiness was due to distinct particle-crushing events, similar to those observed experimentally (Bolton & Cheng, 2001). When one DEM grain broke, microscopic particle rearrangement and redistribution of forces happened at the specific location and triggered a slight variation in the macroscopic volume–stress relationship. This unsteadiness should be eliminated by using a larger soil element. Less fluctuation occurred during unloading because there was then an insignificant amount of particle crushing and rearrangement.

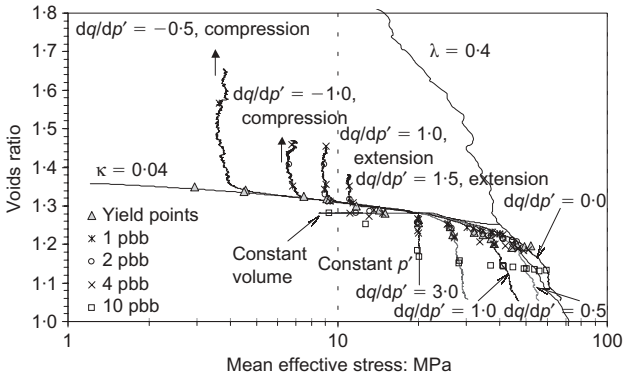

Fig. 5. Projection of pbb surface on voids ratio – $\log p'$ space

On the wet side of critical states (and when the stress ratio, q/p', is low), the volumetric hardening hypothesis of the original Cam-clay framework in e–$\log p'$ space (Roscoe *et al.*, 1958) was found to comply well with the physics of soil regarding elastic deformation, crushing and rearrangement. The pbb contours (or lines of constant granulometry) are approximately parallel to the unloading κ-line. The magnitude of κ should be affected by elasticity at points of contact, surface friction of the spheres and the shape of the agglomerates. On the dry side of critical states (and when the stress ratio is high), the stress paths moved along the κ-line and left the line due to dilation, as bond breakage continued.

Role of crushing

Figure 6 shows the results of a series of simulations that were performed to demonstrate the importance of bond breakage in the shearing mechanism of this DEM soil. The conventional triaxial compression stress path ($\mathrm{d}q/\mathrm{d}p' = 3{\cdot}0$) was adopted. In order to show the influence of particle breakage on soil plasticity, the bond strengths in the simulations indicated as 'elastic plus rearrangement' and 'purely elastic' were increased from the original 4 N to 1×10^{16} N at the beginning of shearing. Additionally, in the simulation indicated 'purely elastic', relative sliding of the grains was also forbidden; the element behaved like a porous elastic solid.

Figure 6(a) shows the stress paths of the three tests plotted in e–$\log p'$ space, whereas Fig. 6(b) shows the stress paths plotted in q–ε_q space. The original normal compression and unloading lines are also plotted in Fig. 6(a) for reference. When bonds were unbreakable, and when no rearrangement of these grains was allowed, the numerical soil experienced a non-linear elastic behaviour and became stiffer at higher stress. It generally followed the κ-line of the e–$\log p'$ plot. When rearrangement of the agglomerates was allowed (elastic plus rearrangement), yielding became possible. However, it resulted in high values of deviator strength, q. It also produced delayed dilation, with the path lying outside the original virgin compression path of the breakable

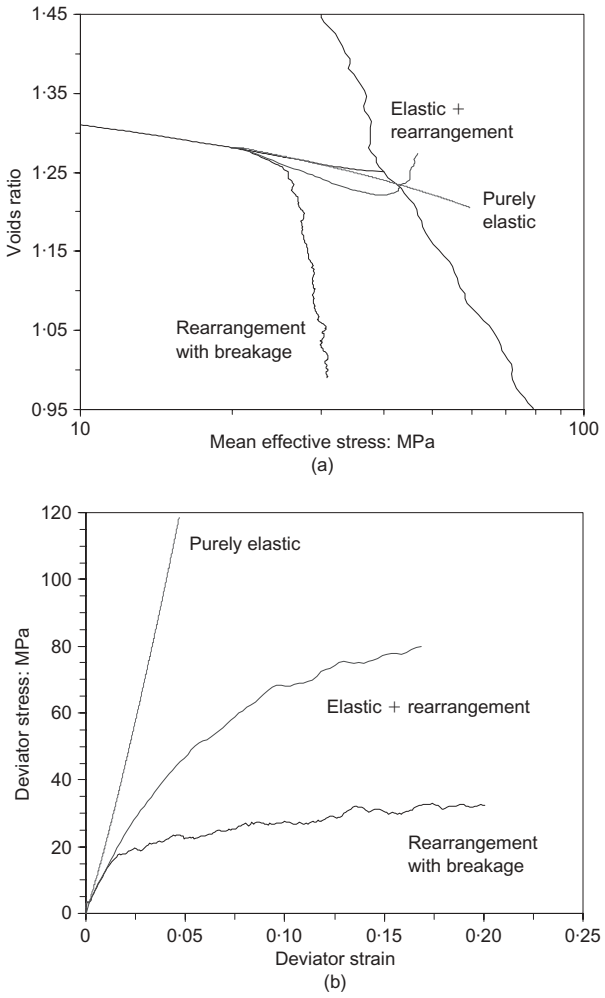

Fig. 6. Effect of breakage and rearrangement on shear behaviour, simulations of conventional triaxial stress path: (a) voids ratio against log mean effective stress; (b) deviator stress against deviator strain

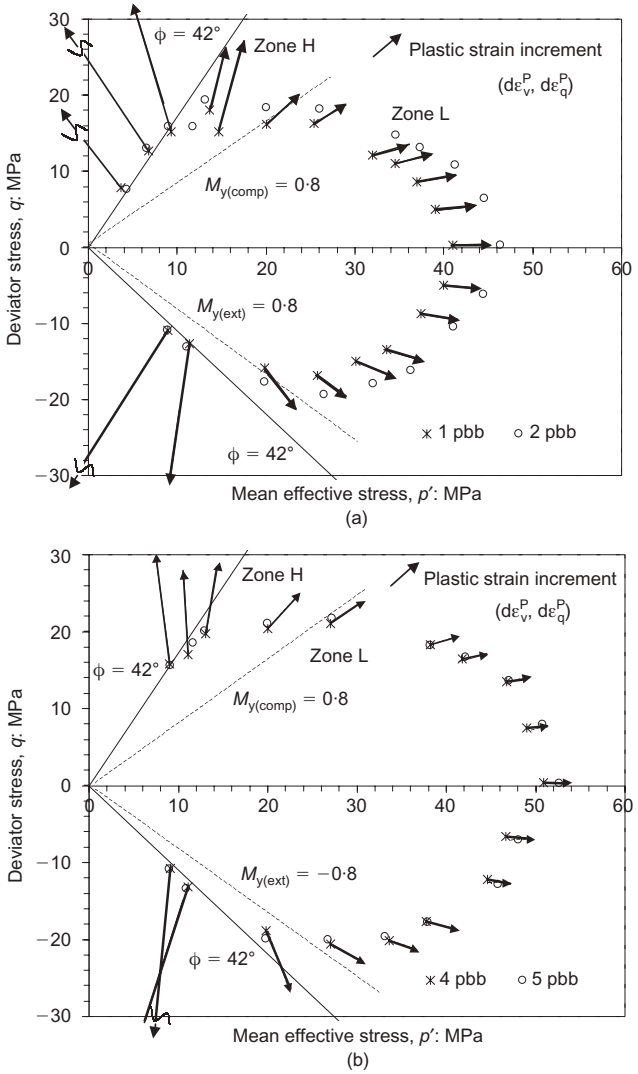

Fig. 7. Plastic strain increment: (a) pbb = 1–2%; (b) pbb = 4–5%

soil. The behaviour can be imagined as shearing an element of rough, stiff rubber balls having a particular shape and size distribution—only suitable for soil mechanics at low stress levels. When the grains were allowed to break and rearrange, behaviour returned to the conventional critical-state framework and sheared towards a reasonable critical state.

PLASTIC DEFORMATION

Plastic deformation was calculated from the measured total macroscopic strain of the element and the derived elastic strain using $\kappa = 0{\cdot}04$ but assuming the elastic deviator strain to be negligible. The plastic strain increments were then plotted in Fig. 7. Similar plastic flow patterns were observed when the DEM element was loaded from 1 pbb to 2 pbb (Fig. 7(a)) and when it was loaded from 4 pbb to 5 pbb (Fig. 7(b)). Both of them showed that the plastic flow followed a non-associated flow rule rather than the normality rule, similar to real soil (e.g. Fig. 4(c)).

The shearing behaviour can be divided into two distinct zones, L and H, characterised by a low and a high absolute magnitude of the stress ratio ($|\eta| = |q|p'|$) respectively. The region of low stress ratio (Zone L) is one of volumetric compaction induced by particle breakage and accompanying rearrangement. For stress paths entering the region of high stress ratio (Zone H), Figs 7(a) and (b) clearly show that the samples first compressed as their state entered Zone H and later dilated when their mobilised angle of friction exceeded 42°. The volume continued to increase, and the grains continued crushing, after the stress point reached its peak in the q–p' stress space. Dilation due to rearrangement of lightly loaded grains, and compaction due to crushing of heavily loaded grains, are opposing tendencies. Therefore plastic deformation in Zone H should follow a different rule from Zone L.

This two-zone shear behaviour resembles the analysis presented by Chandler (1985). By assuming independent microscopic mechanisms of damage and rearrangement, he constructed a plasticity theory that resulted in two regions of contrasting behaviour at yield. One was governed mainly by grain breakage, similar to Zone L described in this paper, whereas the other was governed mainly by rearrangement of grains, similar to Zone H described in this paper. A figure extracted from Chandler (1985) is shown in Fig. 8. Here $\bar{\sigma}$ represents normalised mean stress and $\bar{s}$ represents normalised deviatoric stress respectively. Parameters N and M, emerging from his model, represent normalised dilatancy and normalised internal friction respectively. Chandler shows that different combination of parameters N and M create a wide range of enclosed yield surfaces. His concept of 'critical state' is the point at which the two mechanisms of volume change due to rearrangement and damage cancel out.

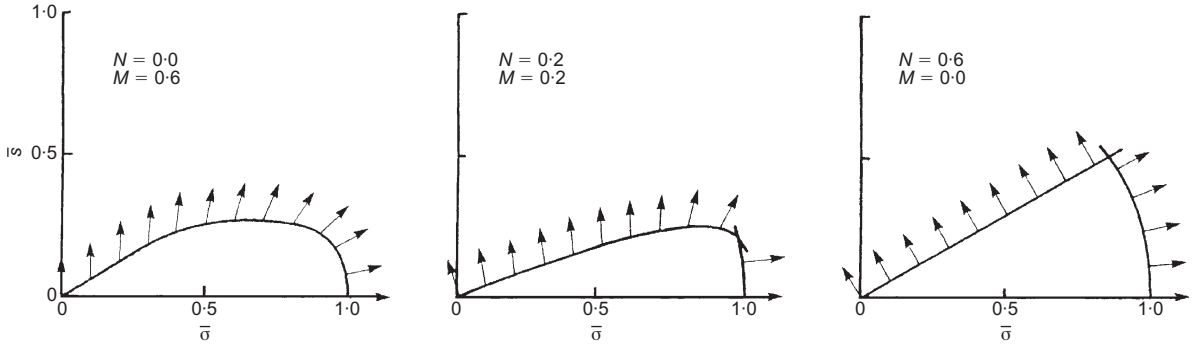

Fig. 8. A plasticity theory without Drucker's postulate (Chandler, 1985)

Flow rule in Zone L

The plastic flow observed in Zone L in the DEM can be represented by a very simple rule, determined only by stress ratio. As normality is not followed, the MCC model cannot be applied without modification.

Examination of the plastic deformation in Figs. 7 (a) and (b) revealed that the ratio of plastic flow increments was approximately proportional to $\eta = q/p'$. Hence the rate of dilatancy in Zone L can be written

$$\frac{1}{\psi} = \frac{\mathrm{d}\varepsilon_q^p}{\mathrm{d}\varepsilon_v^p} = A\eta \tag{1}$$

where ψ is the dilatancy rate as defined by Roscoe & Burland (1968) and A is a proportional constant of this new L-model. Parameter A must be expected to vary with the microstructure of the soil, as it represents the degree to which volume can change when grains break, and the way local rearrangements diffuse to the element boundaries. Fig. 9 indicates the consistency of using this flow rule, taking $A = 0{\cdot}8$ for stress ratios $|\eta| < M_y = 0{\cdot}8$, which defines Zone L. The symmetrical DEM data (on both compression and extension sides) are also well fitted by an elliptical plastic potential surface (PPS; cf. MCC) with a plastic flow rule based on a stress ratio $M_p = 1{\cdot}72$. Outside Zone L, no unique M value could capture the DEM data, as the invariant parameter of stress ratio became the Mohr–Coulomb ϕ value. In the DEM simulations (see Fig. 4(b)), the value of M_y used to scale the elliptical yield surface was found to be approximately $\pm 0{\cdot}8$. If the plastic flow vector is taken to be normal to elliptical potentials, the value of M_p required to scale those potential surfaces is approximately $\pm 1{\cdot}72$, as shown in Fig. 9. If, on the other hand, the parameter A is used to define the plastic flow vectors directly, a value $A \approx 0{\cdot}8$ appears to be acceptable.

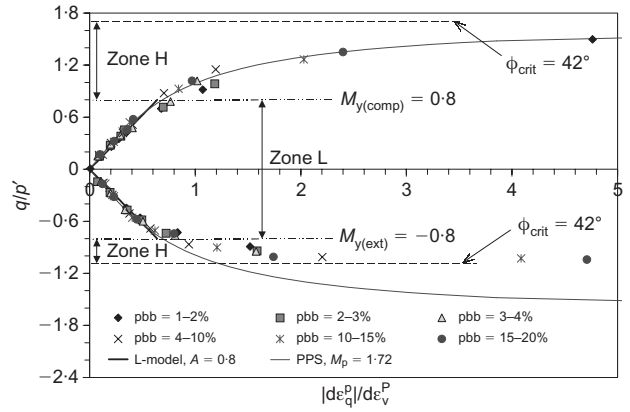

Fig. 9. Stress–dilatancy, Zone L

Plastic deformation in Zone L can therefore be calculated using:

(*a*) the L-model flow-rule or a plastic potential based on the MCC model with an enhanced value $M_p > M_y$
(*b*) the elliptical yield surface scaled by M_y
(*c*) the κ and λ values in e–$\log p'$ space.

The dissipation function can now be determined.

Dissipation in Zone L

The dissipation functions of the original (OCC) and modified Cam-clay (MCC) models can now be compared with our DEM data. Figs. 10(a) and (b) show the dissipation functions of all the DEM data but plotted in a manner allowing a comparison with the two Cambridge models. The best-fit frictional dissipation parameter, $M_{d(OCC)}$, of the OCC

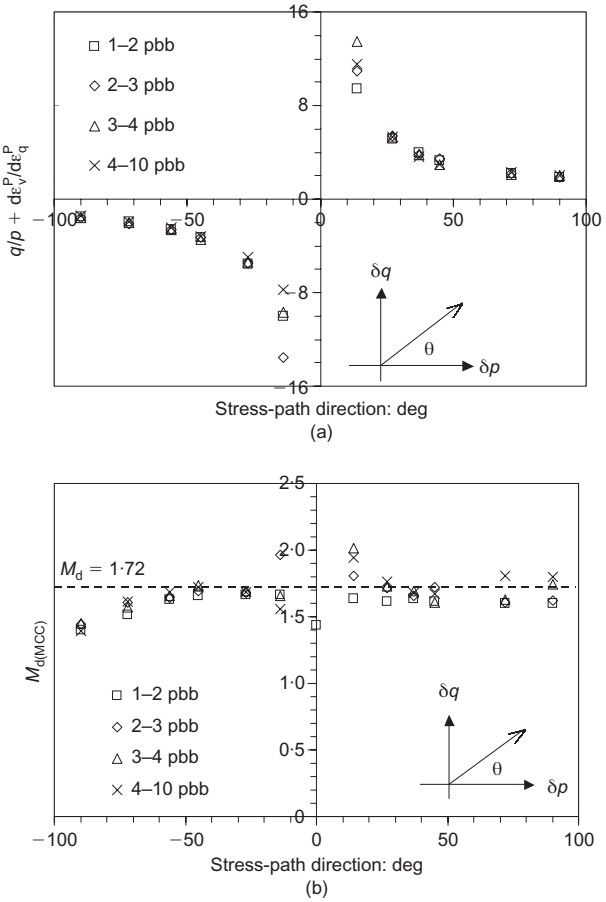

Fig. 10. Dissipation and critical-state parameter: (a) original Cam-clay; (b) modified Cam-clay

was found by rearranging the plastic work and dissipation equation:

$$\frac{q}{p'} + \frac{d\varepsilon_v^p}{d\varepsilon_q^p} = M_{d(OCC)} \quad (2)$$

From Fig. 10(a), this function varied instead of being a constant, M_d. The DEM simulations gave very high values to the rearranged dissipation function (corresponding to the parameter M_d) when θ is small. These high values, found near the p'-axis, were due to the large plastic volumetric strain component. It can be seen that, when the stress-path directions were closer to $\theta = \pm 90°$ (e.g. the constant-p' test), the function decreased asymptotically towards a value of about 1·7, close to the value of M_p that scaled the plastic potential surface. This is because the dissipation is now primarily frictional, with the dilatational term $d\varepsilon_v^p/d\varepsilon_q^p$ being insignificant. The experimental results on which the original Cam-clay model was based were obtained from the simple shear test apparatus (with a path of +90°), the conventional triaxial cell (with a stress path of $\theta = +72°$) or the constant-volume triaxial test (e = constant). In all these cases, the dissipation function modelled by a single critical-state friction parameter, $M_{d(OCC)}$, worked reasonably well. When other stress paths have to be considered, especially those when the crushing effect is more dominant than the frictional effect, a modification is required.

The plastic dissipation equation of the modified Cam-clay model includes the dilatational term in the right-hand-side of the formulation:

$$\frac{q}{p'} + \frac{d\varepsilon_v^p}{d\varepsilon_q^p} = \sqrt{M_{d(MCC)}^2 + \left(\frac{d\varepsilon_v^p}{d\varepsilon_q^p}\right)^2}$$

$$\text{or } \sqrt{\left(\frac{q}{p'} + \frac{d\varepsilon_v^p}{d\varepsilon_q^p}\right)^2 - \left(\frac{d\varepsilon_v^p}{d\varepsilon_q^p}\right)^2} = M_{d(MCC)} \quad (3)$$

Figure 10(b) shows that the rearranged dissipation function, $M_{d(MCC)}$, is reasonably constant in Zone L, although the value decreased slightly on the extension side ($\theta < -70°$). It accounts for the rounded tip on the yield surface around the isotropic axis (stress-path directions are close to $\theta = \pm 0°$) when particle crushing is more significant than shearing. The value of M_d to be used in calculating dissipation at the yield surface is approximately 1·7, which is about double the value of M_y used to describe the shape of the yield surface but equal to the value of M_p that describes the plastic potential function. In the derivation of the OCC and MCC models, of course, these three M values were axiomatically equal, owing to the assumption of normality.

Friction and dilatancy in Zone H

The plastic flow (dilatancy) condition in Zone H (with 'higher' stress ratio, $|\eta| > M_y$) agreed with Rowe's stress–dilatancy theory (Rowe, 1971). He proposed a different representation of the data on the dilation side, in which $KD = R$ for axial compression tests and $K = RD$ for axial extension tests. R is the ratio of major principal stress to minor principal stress, D is $\left(1 - d\varepsilon_v^p/d\varepsilon_a^p\right)$, and K is a constant of proportionality. When plotted according to this relationship in Fig. 11(a), all data passed through the same principal stress ratio, $R = K = 5·0$, at zero volumetric strain rate. This $R = 5·0$ for both compression and extension tests implies $\phi_{crit} = 42°$ at zero volumetric strain rate. This can be compared to the data when plotted in q/p' space in Fig. 9, in which the DEM data converged to ($\eta_{comp} = 1·72$) $\neq$ ($\eta_{ext} = 1·09$) at zero volumetric strain rate. On the other hand, stress–dilatancy does not apply below the M_y lines

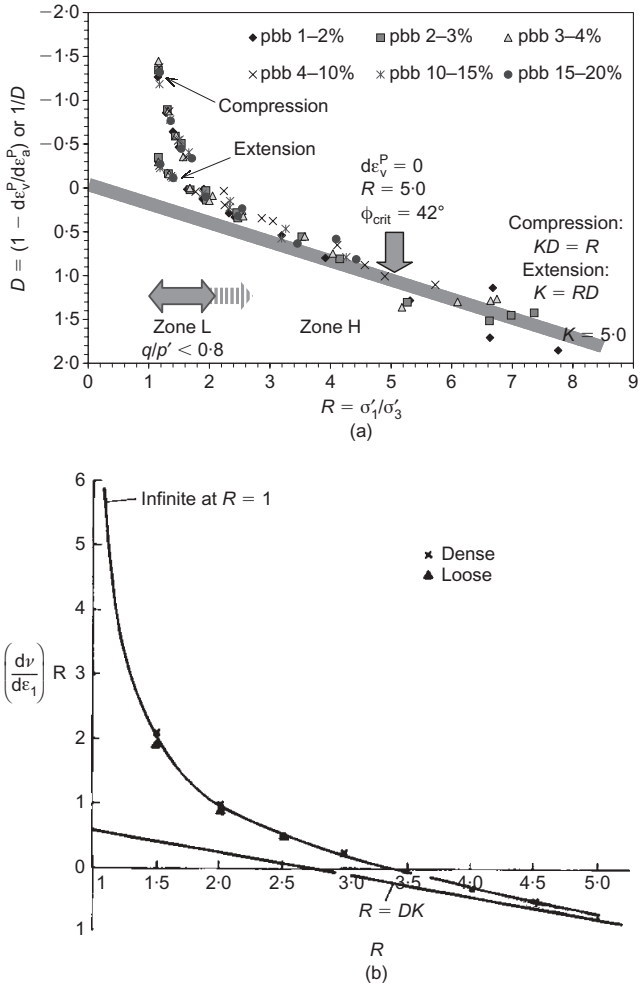

Fig. 11. Stress–dilatancy: (a) Zone H; (b) Rowe's theory (Rowe, 1971)

(Zone L), with $R < 2·1$ or $R < 2·7$ for axial compression or extension tests respectively. A similar plot, Fig. 11(b), can be found in Rowe (1971), although the specific figure described a loading condition with R constant and increasing p'. According to Rowe's theory, the corresponding ϕ_{crit} value is also 42° if $K = \tan^2(45° + \phi_{crit}/2) = 5$.

Figure 12 shows the data for two further sets of DEM simulations of isotropic virgin compression of the DEM elements followed by p'-constant shearing tests of the normally consolidated samples. Fig. 12(a) shows clearly that the element dilated when it was sheared at mean effective stress lower than 7·5 MPa but compacted when sheared at a mean effective stress higher than 7·5 MPa. Recall from Fig. 2(b) that this was the mean effective stress just before the first instance of particle breakage. This mean effective stress represented the critical state of the sample, because the volume change was zero as it sheared. When shearing the DEM crushable soil at other constant mean effective stresses, a unique critical-state zone could be imagined. The slope of the potential critical-state zone has been made consistent with that predicted by the constant-volume DEM tests: see Fig. 11 of Cheng *et al.* (2003). This critical-state line also complied well with that generated by the stress-path tests (Fig. 11(a)) with zero increment of plastic volumetric strain ($d\varepsilon_v^p = 0$). The sample either dilated (shearing at smaller p') or contracted (shearing at higher p') as crushing of soil continued. Fig. 12(b) shows that the secant peak angle of internal friction for samples tested with $p' < p'_{crit} = 7·5$ MPa is higher than $\phi_{crit} = 42°$ and the

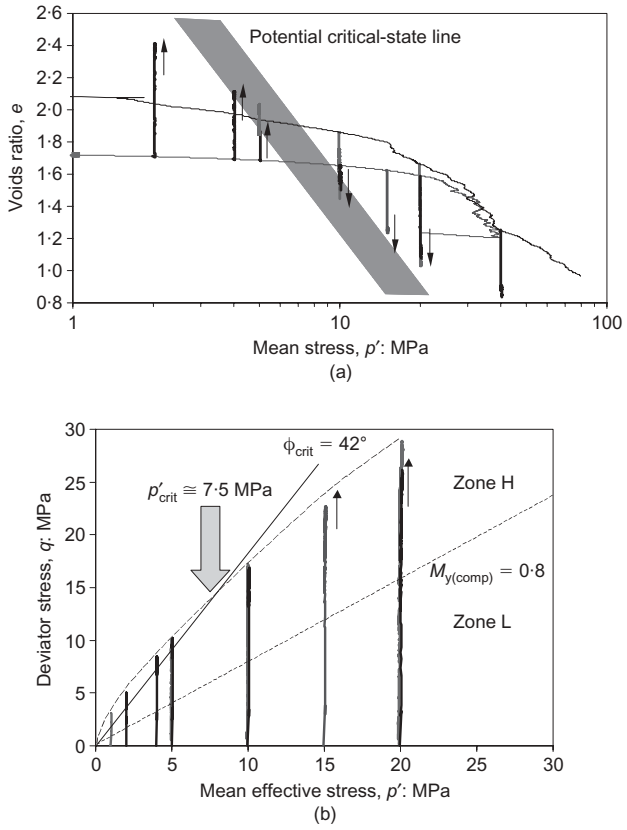

Fig. 12. Critical state of DEM p'-constant tests (Zone H): (a) e–logp' plot; (b) q–p' plot

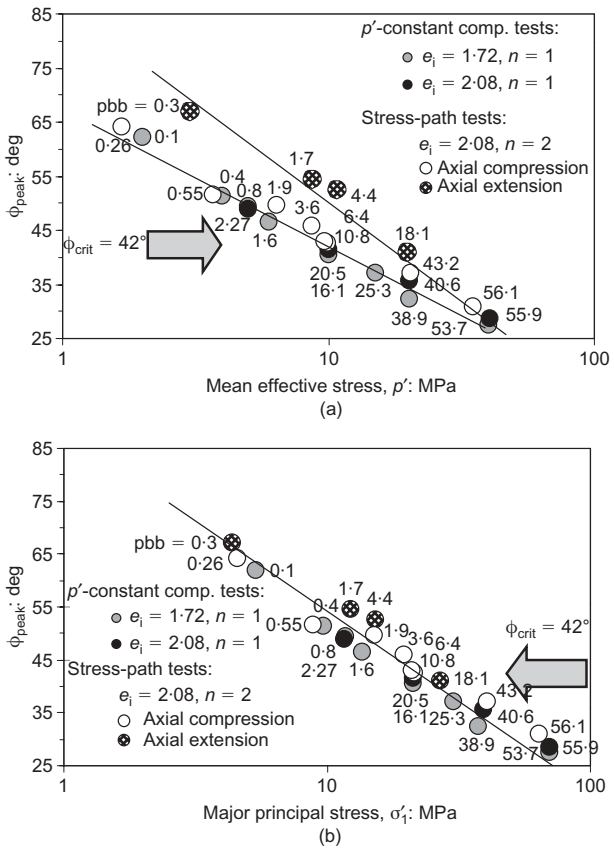

Fig. 13. Peak angle of internal friction (Zone H) against: (a) mean effective stress; (b) major principal stress

strength envelope is curved. The secant peak angle of internal friction with $p' > p'_{crit} = 7{\cdot}5$ MPa is lower than $\phi_{crit} = 42°$ even though the sample was sheared to 40% deviator strain in each case. It is not yet proven whether ongoing shear, crushing and compaction would eventually raise the stress ratio to ϕ_{crit} in that part of Zone H lying below the critical-state line.

Figure 13 illustrates how the peak angle of internal friction (ϕ_{peak}) in Zone H followed a unique rule when stresses increased. At about $p'_{crit} = 7{\cdot}5$ MPa the peak angle of shearing resistance obtained from Fig. 12(b) was equal to 42°. Two different linear relationships for compression and extension tests were found when ϕ_{peak} was plotted with the logarithm of the mean effective stress, p', as shown in Fig. 13(a). However, when the major principal stress (σ'_1) was plotted, the gradient was found to be the same for all data. Fig. 13(b) also shows that the amount of bond breakage (pbb) recorded at peak increases with stress level. The number located near each data point indicates the magnitude of pbb, which increases as the major principal stress increases during all the p'-constant compression tests and the stress-path tests. This implied that particle breakage correlated with the decrease in the peak angle of internal friction, consistent with Bolton (1986). While still in Zone H but with ϕ_{peak} smaller than 42°, the DEM tests seem to show that the maximum angle of internal friction, at least up to 40% shear strain, continues to decrease with the logarithm of stress (see Fig. 13) down towards the angle of interparticle friction, $\phi_\mu = 26{\cdot}6°$. This interesting observation requires further study. Shearing up to such a high percentage of bond breakage may not be realistic, however. A larger number of elementary spheres is required for the DEM 'grain' in order to obtain a realistic comparison with the real sand. Sufficient breakage capacity, and even larger strain, may be required to bring the soil to its ultimate state (Cuccovillo & Coop, 1999).

DISCUSSION

Yield points along numerical stress-path tests were defined by changes of stiffness (Fig. 3), and hardening was quantified by the percentage of bond-breaking (pbb) contours (Fig. 4). Two zones can be distinguished in relation to the overconsolidation ratio n at yield $= p'_{max}/p'$: Zone L for $n < 2$ and Zone H for $n > 2$ (Fig. 7).

At low stress ratio in Zone L, yield surfaces defined either by changes of stiffness, or by contours of breakage, were elliptical and symmetrical about the p' axis on a (q, p') plot, resembling modified Cam-clay (Roscoe and Burland, 1968) (Fig. 4). Moreover, each yield surface in (q, p') space corresponded with an 'elastic' κ-line in (e–logp') space, as envisaged by Roscoe *et al.* (1958) (Fig. 5). The similarities in the shapes of yield surfaces, as well as the similarities in the directions of plastic flow at various levels of shear strain, confirmed the homologous properties of the strain-hardening plastic deformation, and the appropriateness of definitions q and p' to capture both compression and extension test data (Figs 4 and 7). However, the vectors of plastic strain increment clearly disobeyed the normality principle, which was central to all the Cambridge models of soil plasticity, consistently generating more plastic compression than would have been given by associated flow. The lines $M_y = \pm 0{\cdot}8$ that passed through the apexes of the ellipses did not, therefore, coincide with lines of critical states that were found at much higher stress ratios (Fig. 9).

At high stress ratio in Zone H, symmetrical yielding

behaviour in compression and extension is perceived only in terms of the Mohr–Coulomb angle (Fig. 11). The simulations agreed with Rowe's stress–dilatancy model (Rowe, 1971), and confirmed the hypothesis of Bolton (1986) in attributing to grain crushing the observed reduction in peak friction angle with the increase of stress plotted on a logarithmic scale (Fig. 13). The best correlator was the major principal stress, when compression and extension test data were combined. This is also micromechanically reasonable: crushing should occur on strong force chains carrying the major stress. The stress–dilatancy model succeeded both with dilatant and contractile behaviour either side of critical states inside Zone H (Fig. 13). After peak stress ratio, dilatant samples softened towards a critical state. The relatively small number of agglomerates in a test sample, and the 1 : 1 sample shape, precluded the formation of shear bands, however. A critical-state stress ratio, $\phi_{crit} \approx 42°$, was found from stress paths that happened to yield at constant volume (Figs 9, 11 and 12). This angle of internal friction is as high as any found in nature. This may be attributed to the excellent interlocking of the DEM grains, which would be regarded as very rough. The angle of contact friction in the DEM simulations was only $\phi_\mu = 26{\cdot}6°$.

The upward transition in stress ratio from $M_y = 0{\cdot}8$ defining yield surfaces in Zone L to $\phi_{crit} \approx 42°$ defining shear at constant volume in Zone H is noteworthy. The elliptical yield surface is still apparently valid (Fig. 4), but the flow rule changes to that of Rowe, and the criterion for stress ratio changes from q/p' to ϕ (Figs 7 and 11). In detail, the trial use of $\phi_\mu = 26{\cdot}6°$ as a separator (instead of $M_y = 0{\cdot}8$) between Zones L and H is also quite successful, corresponding as it does to $M_\mu = 1{\cdot}05$ in compression, and $M_\mu = -0{\cdot}78$ in extension, or $R = 2{\cdot}6$ in both compression and extension (Figs 9 and 11). Although the correspondence may be coincidental, it seems micromechanically appropriate. Samples yielding with $\phi < \phi_\mu$ are dominated by crushing and consequential local rearrangement but global sliding cannot occur, whereas samples yielding with $\phi > \phi_\mu$ do suffer global sliding mechanisms of the sort envisaged by Rowe. Note, however, that all yielding behaviour, whether in Zone L or Zone H, is strongly influenced by grain crushing.

CONCLUSIONS

(*a*) This paper, following the work of Cheng *et al.* (2003), applies the same method of generating numerical 'grains' within a DEM simulation in order to model the behaviour of soil in a wide range of stress-path tests. The creation of an arbitrary number of identical but virtual soil samples, in which attributes such as grain friction, grain crushing strength, or stress path can be varied selectively, is a powerful tool to understand the physical origins of soil behaviour. In this study, grain crushing has been confirmed to be a key physical principle underlying soil plasticity.

(*b*) For DEM samples that are lightly overconsolidated at yield, yield surfaces are contours of grain breakage, and hardening is clastic in the sense of Bolton & McDowell (1998). Modified Cam Clay successfully describes behaviour except that normality was not observed. The M_y value controlling the *shape* of the elliptical yield surfaces was about half that of the M_d value evaluating friction dissipation *on* the yield surface.

(*c*) For samples that are more heavily overconsolidated at yield, the stress dilatancy models of Rowe (1971) and Bolton (1988) successfully married with the results. Grain breakage was confirmed as the reason for the peak friction angle decreasing with increase of stress. The major principal stress was a better correlator than the mean stress, when extension and compression data were combined. All angles of friction were as high, or somewhat higher than, values associated with the most frictional granular aggregates. This is attributed to the rough shapes of the DEM grains, which are capable of strong interlocking.

(*d*) The DEM simulations therefore created data identical in form to the laboratory triaxial tests that were originally used to support the various theories of plastic soil behaviour created by Roscoe, Rowe, Schofield, Burland, Bolton, Chandler and others. They replicated the partial successes of each approach and also demonstrated the dissonance between them that is evident in real soil data. The DEM technique may therefore permit the detailed mapping of plastic soil behaviour in terms of the physical characteristics of grains. This has been achieved only by permitting grains to crush. In future, the technique will be used to study the effects of surface roughness, granulometry, anisotropy and other manifestations of soil fabric that currently lead to confusion in the interpretation of soil performance observed in triaxial tests.

NOTATION

A	proportional constant for flow rule of the new model at Zone L
D	dilatancy rate $= 1 - \mathrm{d}\varepsilon_v^p/\mathrm{d}\varepsilon_a^p$ (Rowe, 1971)
e	voids ratio
e_i	initial voids ratio of a specific isotropic compression curve
F	critical state stress ratio, q/p'
K	proportional constant $= \tan^2(45 + \phi_{crit}/2)$ in $R = KD$ (Rowe, 1971)
M	critical-state friction parameter (Roscoe *et al.*, 1963)
M, N	microscopic parameter defined by Chandler (1985) to define the relative importance between rearrangement and particle crushing
M_d	stress ratio, q/p', related to the dissipation function
M_p	stress ratio, q/p', related to the plastic potential surface
M_y	stress ratio, q/p', at peak deviator stress of a yield surface ($M_{y(comp)}$ or $M_{y(ext)}$)
n	overconsolidation ratio
pbb	percentage of simple contact bonds broken counted from the beginning of shearing
p'	mean effective stress
p'_i	mean effective stress before stress-path shear tests
p'_{max}	maximum pre-compression pressure before isotropic unloading
p'_0	peak mean effective stress of a specific yield surface
$\mathrm{d}p'$	change in mean effective stress
q	deviator stress, $\sigma'_1 - \sigma'_3$
$\mathrm{d}q$	change in deviator stress
R	ratio of major to minor principal effective stress (σ'_1/σ'_3)
Y_2	kinematic sub-yield surface (Smith *et al.*, 1992)
Y_3	envelope of initial boundary surface (Smith *et al.*, 1992)
ε_1	major principal strain
ε_3	minor principal strain
ε_q	deviator strain, $2/3(\varepsilon_1 - \varepsilon_3)$
$\mathrm{d}\varepsilon_a^p$	increment of plastic axial strain $[\mathrm{d}\varepsilon_a^p = (\mathrm{d}\varepsilon_v^p + 3\mathrm{d}\varepsilon_q^p)/3]$
$\mathrm{d}\varepsilon_q^p$	increment of plastic deviator strain
$\mathrm{d}\varepsilon_v^p$	increment of plastic volumetric strain
η	stress ratio, q/p'
θ	stress-path direction from p'-axis $= \tan^{-1}(\mathrm{d}q/\mathrm{d}p')$
κ	elastic parameter of isotropic unloading (Roscoe *et al.*, 1958)
λ	isotropic hardening parameter of virgin compression line (Roscoe *et al.*, 1958)
μ	coefficient of friction of sphere
σ'_1	major principal stress acting on cubical sample or triaxial cell

σ'_3 minor principal stress acting on cubical sample or triaxial cell
ϕ angle of shearing resistance, $\sin\phi = 2|M_{comp}|/(6 + |M_{comp}|)$ or $\sin\phi = 3|M_{ext}|/(6 - |M_{ext}|)$
ϕ_{crit} critical-state angle of shearing resistance
ϕ_{peak} peak mobilised angle of shearing resistance
ϕ_μ angle of friction at surface of DEM spheres (input parameter of DEM simulations)
ψ dilatancy rate $= d\varepsilon_v^p/d\varepsilon_q^p$ (Roscoe and Burland, 1968)

REFERENCES

Bolton, M. D. (1986). The strength and dilatancy of sands. *Géotechnique* **36**, No. 1, 65–78.

Bolton, M. D. & Cheng, Y. P. (2001). Micro-geomechanics (plus Discussion). *Proceedings of the workshop on constitutive and centrifuge modelling: Two extremes*, Monte Verita, July 2001, pp. 59–74.

Chandler, H. W. (1985). A plasticity theory without Drucker's postulate, suitable for granular materials. *J. Mech. Phys. Solids* **33**, No. 3, 215–226.

Cheng, Y. P. (2004). *A micro-mechanical modelling of soil plasticity.* PhD dissertation, Cambridge University.

Cheng, Y. P., Nakata, Y. & Bolton, M. D. (2003). Distinct element simulation of crushable soil. *Géotechnique* **53**, No. 7, 633–641.

Cuccovillo, T. & Coop, M. R. (1999). On the mechanics of structured sands. *Géotechnique* **49**, No. 6, 741–760.

Gajo, A. & Wood, D. M. (1999). Severn-Trent sand: a kinematic-hardening constitutive model: the *q-p* formulation. *Géotechnique* **49**, No. 5, 595–614.

Jardine, R. J. (1992). Some observations on the kinematic nature of soil stiffness. *Soils Found.* **32**, No. 2, 111–124.

McDowell, G. R. & Harireche, O. (2002). Discrete element modelling of soil particle fracture. *Géotechnique* **52**, No. 2, 131–135.

McDowell, G. R. & Bolton, M. D. (1998). On the micromechanics of crushable aggregates. *Géotechnique*, **48**, No. 5, pp. 667–679.

McDowell, G. R., Bolton, M. D. & Robertson, D. (1996). The fractal crushing of granular materials. *Int. J. Mech. Phys. Solids* **44**, 2079–2102.

Mroz, Z., Norris, V. A. & Zienkiewicz, O. C. (1979). Application of an anisotropic hardening model in the analysis of elasto-plastic deformation of soils. *Géotechnique* **29**, No. 1, 1–34

Robertson, D. (2000). *Computer simulations of crushable aggregates*. PhD dissertation, Cambridge University.

Roscoe, K. H. & Burland, J. B. (1968). On the generalized stress–strain behaviour of 'wet' clay. In *Engineering plasticity* (eds J. Heyman and F. A. Leckie), pp. 535–609. Cambridge: Cambridge University Press.

Roscoe, K. H., Schofield, A. N. & Wroth, M. A. (1958). On the yielding of soils. *Géotechnique* **8**, 22–53.

Roscoe, K. H., Schofield, A. N. & Thurairajah A. (1963). Yielding of clays in states wetter than critical. *Géotechnique* **13**, 211–240.

Rowe, P. W. (1971) Theoretical meaning and observed values of deformation parameters for soil. In *Stress–strain behaviour of soils, Proceedings of Roscoe Memorial Symposium*, Cambridge University, (ed. R. H. G. Parry), pp. 143–194.

Schofield, A. N. & Wroth, C. P. (1968) *Critical state soil mechanics.* London: McGraw-Hill.

Smith, P. R., Jardine, R. J. & Hight, D. W. (1992) The yielding of Bothkennar clay. *Géotechnique* **42**, No. 2, 257–274.